# Simultaneous dual-band ultrahigh-resolution full-field optical coherence tomography

Delphine Sacchet, Julien Moreau, Patrick Georges, Arnaud Dubois

# Simultaneous dual-band ultra-high resolution full-field optical coherence tomography

**Delphine Sacchet[*], Julien Moreau, Patrick Georges, and Arnaud Dubois**

*Laboratoire Charles Fabry de l'Institut d'Optique, CNRS UMR 8501, Université Paris-Sud,
Campus Polytechnique, RD128, 91127 Palaiseau Cedex, France*
*[*]Corresponding author: delphine.sacchet@institutoptique.fr*

**Abstract**: Ultrahigh-resolution full-field optical coherence tomography (FF-OCT) is demonstrated in the 800 nm and 1200 nm wavelength regions simultaneously using a Silicon-based (Si) CCD camera and an Indium Gallium Arsenide (InGaAs) camera as area detectors and a halogen lamp as illumination source. The FF-OCT setup is optimized to support the two broad spectral bands in parallel, achieving a detection sensitivity of ~ 90 dB and a micrometer-scale resolution in the three directions. Images of *ex vivo* biological tissues are presented (rabbit trachea and *Xenopus laevis* tadpole) with an increase in penetration depth at 1200 nm. A color image representation is applied to fuse both images and enhance spectroscopic property visualization.

© 2008 Optical Society of America

**OCIS codes**: (170.4500) Optical Coherence Tomography; (170.3880) Medical and biological imaging; (170.3890) Medical optics instrumentation; (170.6510) Spectroscopy, tissue diagnostics; (180.3170) Interference microscopy.

---

## Reference and links

1. D. Huang, E. A. Swanson, C. P. Lin, J. S. Schuman, W. G. Stinsin, W. Chang, M. R. Hee, T. Flotte, K. Gregory, C. A. Puliafito, and J. G. Fujimoto, "Optical coherence tomography," Science **254**, 1178-1181 (1991).
2. A. F. Fercher, "Optical coherence tomography," J. Biomed. Opt. **1**, 157-173 (1996).
3. E. A. Swanson, J. A. Izatt, M. R. Hee, D. Huang, C. P. Lin, J. S. Schumann, C. A. Puliafito, and J. G. Fujimoto, "*In-vivo* retinal imaging by optical coherence tomography," Opt. Lett. **18**, 1864-1866 (1993).
4. G. J. Tearney, B. E. Bouma, S. A. Boppart, B. Golubovic, E. A. Swanson, and G. J. Fujimoto, "Rapid acquisition of *in-vivo* biological images by use of optical coherence tomography," Opt. Lett. **21**, 1408-1410 (1996).
5. J. G. Fujimoto, "Optical coherence tomography for ultrahigh resolution *in-vivo* imaging," Nat. Biotechnol. **21**, 1361-1367 (2003).
6. L. Vabre, A. Dubois, and A. C. Boccara, "Thermal-light full-field optical coherence tomography," Opt. Lett. **27**, 530-533 (2002).
7. A. Dubois, K. Grieve, G. Moneron, R. Lecaque, L. Vabre, and A. C. Boccara, "Ultrahigh-resolution full-field optical coherence tomography," Appl. Opt. **43**, 2874 (2004).
8. W. Y. Oh, B. E. Bouma, N. Iftimia, S. H. Yun, R. Yelin, and G. J. Tearney, "Ultrahigh-resolution full-field optical coherence microscopy using InGaAs camera," Opt. Express **14**, 726-735 (2006).
9. A. Dubois, G. Moneron, and A. C. Boccara, "Thermal-light full-field optical coherence tomography in the 1.2 µm wavelength region," Opt. Commun. **266**, 738-743 (2006).
10. A. Dubois, G. Moneron, K. Grieve, and A. C. Boccara, "Three-dimensional cellular-level imaging using full-field optical coherence tomography," Phys. Med. Biol. **49**, p. 1227-1234 (2004).
11. B. Laude, A. De. Martino, B. Drévillon, L. Benattar, and L. Schwartz, "Full-field optical coherence tomography with thermal light," Appl. Opt. **41**, 2059-2064 (2002).
12. J. Na, W. J. Choi, E. S. Choi, S. Y. Ryu, and B. H. Lee, "Image restoration method based on Hilbert transform for full-field optical coherence tomography," Appl. Opt. **47**, 459-466 (2008).
13. U. Morgner, W. Drexler, F. X. Kärtner, X. D. Li, C. Pitris, E. P. Ippen, and G. J. Fujimoto, "Spectroscopic optical coherence tomography," Opt. Lett. **25**, 111-113 (2000).
14. D. C. Adler, T. H. Ko, P. R. Herz, and J. G. Fujimoto, "Optical coherence tomography contrast enhancement using spectroscopic analysis with spectral autocorrelation," Opt. Express **12**, 5489-5501 (2004).

15. D. J. Faber, E. G. Mik, M. C. G. Aalders, and T. G. van Leeuwen, "Toward assessments of blood oxygen saturation by spectroscopic optical coherence tomography," Opt. Lett. **30**, 1015-1017 (2005).
16. A. Dubois, J. Moreau, and A. C. Boccara, "Spectroscopic ultrahigh-resolution full-field optical coherence microscopy," Opt. Express **16**, 17082-17091 (2008).
17. V. M. Gelikonov, G. V. Gelikonov, and F. I. Feldchtein, "Two-wavelength optical coherence tomography," Radiophys. Quantum Electron. **47**, 848-859 (2004).
18. Y. Pan and D. L. Farkas, "Noninvasive imaging of living human skin with dual-wavelength optical coherence tomography in two and three dimensions," J. Biomed. Opt. **3**, 446-455 (1998).
19. F. Spöler, S. Kray, P. Grychtol, B. Hermes, J. Bornemann, M. Först, and H. Kurz, "Simultaneous dual-band ultra-high resolution optical coherence tomography," Opt. Express **15**, 10832-10842 (2007).
20. A. D. Aguirre, N. Nishizawa, W. Seitz, M. Ledere, D. Kopf, and J. G. Fujimoto, "Continuum generation in a novel photonic crystal fiber for ultrahigh resolution optical coherence tomography at 800 nm and 1300 nm," Opt. Express **14**, 1145-1160 (2006).
21. D. M. Gale, M. I. Pether, and J. C. Dainty, "Linnik microscope imaging of integrated circuit structures," Appl. Opt **35**, 131-148 (1996).
22. A. Dubois, L. Vabre, A. C. Boccara, and E. Beaurepaire, "High-resolution full-field optical coherence tomography with a Linnik microscope," Appl. Opt. **41**, 805-812 (2002).
23. G. M. Hale and M. R. Querry, "Optical constants of water in the 200 nm – 200 µm wavelength region," Appl. Opt **12**, 555-563 (1973).
24. Y. Coello, B. Xu, T. L. Miller, V. V. Lozovoy, and M. Dantus, "Group-velocity dispersion measurements of water, seawater and ocular components using multiphoton intrapulse interference scan phase," Appl. Opt. 46, 3894-8401 (2007).
25. P. Parsa, S. L. Jacques, and N. S. Nishioka, "Optical properties of rat liver between 350 and 2200 nm," Appl. Opt. **28**, 2325-2330 (1989).
26. J. M. Schmitt, A. Knuttel, M. Yadlowsky, and M. A. Eckhaus, "Optical coherence tomography of a dense tissue: statistics of attenuation and backscattering," Phys. Med. Biol. **39**, 1705-1720 (1994).
27. S. T. Flock, S. L. Jacques, B. C. Wilson, W. M. Star, and M. J. C. van Gemert, "Optical properties of Intralipid: a phantom medium for light propagation studies," Lasers Surg. Med. **12**, 510-519 (1992).
28. H. G. van Staveren, C. J. M. Moes, J. van Marle, S. A. Prahl, and M. J. C. van Gemert, "Light scattering in Intralipid-10% in the wavelength range of 400-1100 nanometers," Appl. Opt. **30**, 4507-4515 (1991).

## 1. Introduction

Optical coherence tomography (OCT) is a well-established optical imaging technique that uses low-coherence interferometry to produce micrometer-scale resolution images of biological media [1-2]. Since its first application in examination of pathologic changes of the retina morphology [3], the range of applications of OCT has largely increased especially in the biomedical field [4-5].

Full-field optical coherence tomography (FF-OCT), also sometimes referred to as full-field optical coherence microscopy, was introduced a few years ago as an alternative method to conventional OCT using an interference microscope and a camera as an array detector combined with a low coherence illumination source for parallel acquisition of *en-face* oriented tomographic images [6-9]. FF-OCT is a technique of choice for noninvasive three-dimensional imaging of *ex vivo* biological tissues with ultra-high (~ 1 µm) spatial resolution [10]. FF-OCT is based on phase-shifting interferometry: several interferometric images (frames) are acquired with an image sensor, a phase-shift being introduced between each of these frames by using, for example, the displacement of the reference mirror. The amplitude of the interference signal, i.e. the fringe envelope, is calculated by combination of these frames. A number of phase-shifting methods have been proposed using 2, 4 or 7 frames with steps or sinusoidal phase modulations [7, 9-12].

Recent developments in OCT technology have been carried out in order to exploit the spectroscopic response of the imaged sample. This technique, referred to as spectroscopic OCT, detects and processes the interferometric signal to provide spatially-resolved spectroscopic information. It can be used to enhance image contrast, permitting better differentiation of tissues through their spectroscopic properties and providing additional information on the sample composition [13-16]. An alternative method to take advantage of the spectroscopic response of the sample is to image at several distinct wavelengths. Recently,

dual-band OCT was demonstrated at ~ 800 nm and ~ 1200-1300 nm using supercontinuum generation in non-linear crystal fibers [17-20].

In this paper, we report on dual-band ultrahigh-resolution FF-OCT in the 800 nm and 1200 nm wavelength regions simultaneously, by use of two area cameras and a halogen lamp as low coherence illumination source. Silicon-based (Si) cameras are commonly used in FF-OCT to probe the 600 - 1000 nm wavelength region [6-7]. For wavelengths larger than 1000 nm, Si cameras are replaced by Indium Gallium Arsenide (InGaAs) cameras because of their efficient wavelength response in the 900 - 1700 nm band [8-9]. We present the full-field OCT setup, which supports both wavelength bands in parallel with a micrometer-scale imaging resolution. The performances of our system in terms of spatial resolution and detection sensitivity are reported. A highly-contrasted object embedded in a scattering medium and several biological tissues have been imaged in both wavelength regions simultaneously.

## 2. Methods

### 2.1 Experimental setup

The experimental setup of our simultaneous dual-band ultrahigh-resolution full-field OCT system is represented schematically in Fig. 1.
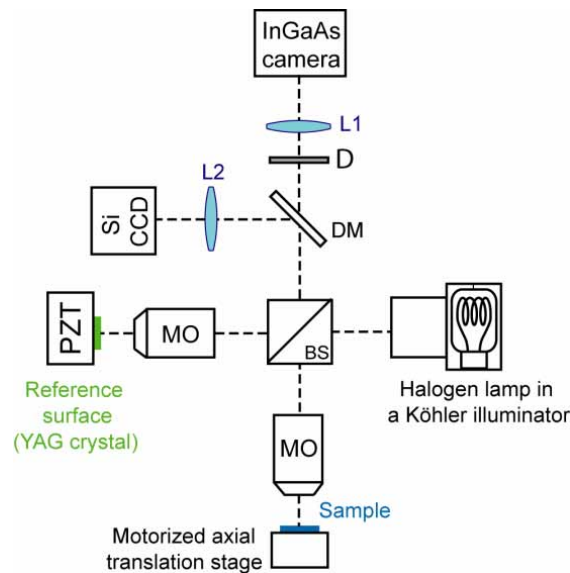


Fig. 1. Schematic representation of the dual-band FF-OCT setup. BS, broadband beam splitter; MO, vertically-positioned microscope objectives; L1, L2, aplanetic doublet achromat lenses (300-mm focal length, L1 infrared optimized and L2 near-infrared optimized); DM dichroic mirror, D density; PZT, piezoelectric stage actuator.

The setup is based on a Michelson interferometer with identical water-immersion microscope objectives in both arms. This configuration is referred to as the Linnik interference microscope [21-22]. The use of water-immersion microscope objectives avoids focusing adjustments between the coherence plane and the focal plane [9], minimizes dispersion mismatch in the interferometer arms [7], reduces light reflection from the sample surface, and also preserves the biological sample. The microscope objectives used in our experiment (10×, 0.3 numerical aperture and 3 mm working distance, from Olympus) are not optimized in the 1200 nm wavelength region. Their transmission drops from 81% at 800 nm to 59% at 1200 nm. Moreover, optical aberrations are not well corrected, which degrades the image contrast and resolution. The light source is a 100 W tungsten halogen lamp, with a

stabilized power supply, incorporated in a Köhler illuminator setup for homogeneous illumination of the whole microscope objective fields. Light is split into the reference and sample arms by a broadband beam splitter, with a variation of the ratio transmission/reflection less than 10% in the entire wavelength region of interest (700 - 1600 nm). A polished surface of an $Y_3Al_5O_{12}$ (YAG) crystal is placed in the reference arm of the Linnik interferometer at the focus of the microscope objective. This reference surface provides 2.5% of reflectivity in water for both wavelength regions. A motorized axial translation stage in the sample arm allows axial scanning of the sample to acquire *en-face* images at different depths. A dichroic mirror with high reflectivity (>98%) in the 650-950 nm band and high transmission (>85%) in the 1100 -1500 nm is used to separate both spectral bands before detection. Two achromatic lenses are used to project simultaneously the interferometric images onto two camera arrays, a silicon CCD camera (Model CA-D1 from Dalsa, 256×256 pixels, 8 bits, 180 Hz) with a maximal sensitivity at ~ 800 nm (650 – 950 nm wavelength region) and an InGaAs area scan camera (Model SU320MS from Sensors Unlimited, 320×256 pixels, 12 bits, 20 Hz) with a maximal sensitivity at ~ 1300 nm (900 – 1700 nm wavelength region). Each lens is optimized at infinite conjugate ratios for the spectral region of its associated camera (650 – 1050 nm for the lens in front of the Si camera and 1050 – 1620 nm for the lens in front of the InGaAs camera). Because of chromatic aberrations in the infrared, the microscope objectives have different focus planes for both wavelength bands. The lens L1 used to project the images onto the InGaAs camera is therefore slightly moved forward compared to the lens L2 (~ 20 mm) in order to have an image in focus simultaneously on the two cameras. This displacement causes negligible additional optical aberrations considering the depth of field of L1. An optical density is set ahead the InGaAs camera to work close to saturation simultaneously for both cameras.

*2.2 Image acquisition*

*En-face* tomographic images are produced using a phase-shifting method requiring the acquisition of only two phase-opposed interferometric images [10]. The reference mirror is mounted on a piezoelectric stage actuator (PZT) to make it oscillate at the frequency *f*. This oscillation generates a sinusoidal phase modulation of amplitude ψ. The signal delivered by each pixel of each camera can be expressed as a function of time as

$$I(t) = \bar{I} + I_{coh} \cos\left[\phi + \psi \sin(2\pi f t)\right], \tag{1}$$

where $\bar{I}$ represents the average signal intensity, $\phi$ the optical phase and $I_{coh}$ the intensity of the coherent signal, proportional to the amplitude of light backscattered by the sample structures located in the coherence volume. $I_{coh}$ is the signal that must be extracted to produce *en-face* tomographic images.

In single-band FF-OCT, the camera is synchronized with the PZT oscillation and triggered at the frequency 2*f*, in order to capture two images per modulation period $T = 1/f$ [10]. A number *N* of series of two images is accumulated to increase the signal-to-noise ratio. The two accumulated images ($I_1$, $I_2$) correspond to *N* times the integration of the signal over the two halves of the modulation period, in parallel for all pixels of the camera:

$$I_1 = \eta N \int_0^{T/2} I(x,y,t)dt \quad \text{and} \quad I_1 = \eta N \int_{T/2}^{T} I(x,y,t)dt \tag{2}$$

where $\eta$ is the quantum efficiency of the camera.

The tomographic image is calculated from the squared difference of these two images:

$$\left(I_1 - I_2\right)^2 \cong I_{coh}^2 \sin^2 \phi \left(\eta N f\right)^2 \tag{3}$$

Actually, the fringe envelope $I_{coh}$ is not truly extracted since the phase $\phi$ is not eliminated. A phase-shifting method using a combination of more than two interferometric images is required to eliminate it, but would decrease the acquisition speed. Moreover, due to the size and distribution of the structures in most biological samples, the fringes are generally not visible in the images.

In our dual-band FF-OCT system, because the cameras do not operate at the same frequency, simultaneous imaging is not as straightforward. The frame rate and the exposure time of each camera must be adjusted to appropriate values.

For maximal operation speed, the PZT oscillation frequency is set to be equal to half the frame rate of the fastest camera (the Si camera). Since the InGaAs camera is slower than the Si camera, its frame rate has to be a multiple of the Si camera frame rate, as described schematically in Fig. 2:

$$f(Si) = nf(InGaAs) = 2f(piezo) \Leftrightarrow 2nT(Si) = 2T(InGaAs) = nT(piezo) , \qquad (4)$$

where $n$ is an integer. Successive images acquired by the InGaAs camera are phase-opposed only if $n$ is an odd integer (see Fig. 2(b) and 2(c)). Thus, with a proper synchronization between the PZT oscillation and the triggered signal of both cameras, the Si camera acquires $2n$ phase-opposed images during $n$ oscillations of the PZT, while the InGaAs acquires only two phase-opposed images. We selected electronically a frame rate of 180 Hz for the Si camera and 20 Hz for the InGaAs camera. With those parameters, the frequency of the PZT oscillation is 90 Hz and $n = 9$.

In continuous phase-shifting methods, the images are integrated while the phase changes, which induces a slight degradation of the interference contrast. This contrast degradation, which depends on the exposure time and not on the camera frame rate, has to be identical for both acquisition systems for fair comparison of the tomographic images. For that purpose, the exposure time is selected electronically equal to 2.05 ms for both cameras (maximal acquisition time of the fastest camera).
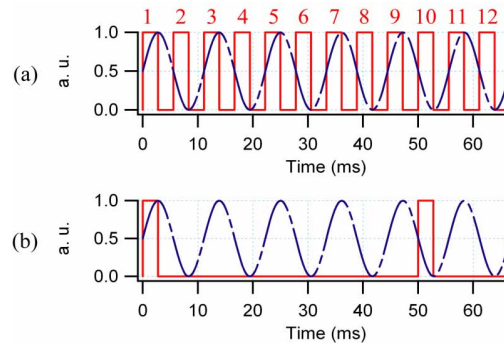


Fig. 2. Timing diagram of the acquisition system of dual-band FF-OCT. The red curves correspond to the synchronization signal of cameras and the blue dotted curves correspond to the PZT oscillation. (a) Si camera. (b) InGaAs camera.

## 3. System characteristics

### 3.1 Detection sensitivity

Detection sensitivity is a crucial parameter in OCT, because it determines the imaging contrast and penetration depth. Assuming a camera operating close to saturation and being shot-noise limited, the smallest detectable reflectivity of our FF-OCT system is [7]:

$$R_{\min} = \frac{\left(R_{ref} + R_{inc}\right)^2}{2N\xi_{sat}R_{ref}} , \qquad (5)$$

where $\xi_{sat}$ represents the full-well capacity of the camera pixels, $N$ is the number of accumulated images, $R_{ref}$ is the reflectivity of the reference surface and $R_{inc}$ is the proportion of incoherent light, resulting essentially from backscattering and backreflection by structures within the biological media localized outside the coherence volume.

In the experiment setup, a great care was taken to minimize the incoherent light. In particular, all the optical components are antireflection coated. We have measured that the incoherent light coming from the setup without biological sample represents a reflectivity of 0.02%. When a biological sample is imaged, the reflection on the sample surface is minimized by index matching, using water-immersion objectives. The incoherent light coming from the biological sample ranges between 0.4% and 0.8% typically. Measurements of the detection sensitivity with both cameras without biological sample are reported in Fig. 3. Detection sensitivity of the order of 90 dB is easily achievable with both cameras even by considering degradation caused by the incoherent light coming from a biological sample ($\sim 3$ dB). The straight lines correspond to the shot-noise limit calculated from Eq. (5) with a full-well capacity $\xi_{sat} \sim 1{\times}10^5$ electrons for the Si camera and $\xi_{sat} \sim 8{\times}10^5$ electrons for the InGaAs camera, a reflectivity $R_{ref}{\sim}2.5\%$ for the reference surface and an equivalent reflectivity $R_{inc}{\sim}0.02\%$ for the incoherent light. The difference between experimental results and shot-noise limit for the InGaAs camera ($\sim 2$ dB) results from a residual electrical noise for this camera. For large numbers of accumulated images, we can notice a saturation of the detection sensitivity. Indeed, a large number of accumulated images corresponds to a long time acquisition, for which the setup is more sensitive to mechanical drifts.

In order to study the effect of wavelength on biological imaging, detection sensitivities have to be equal in both bands. According to Eq. (5), this can be achieved by adjusting the number of images accumulated by each camera. In the rest of the study, we have chosen a detection sensitivity of $\sim 90$ dB, which requires the accumulation of 250 images with the Si camera and 50 images with the InGaAs camera. These numbers of accumulated images correspond to an acquisition time of 2.5 and 5 s for the Si and InGaAs cameras respectively to produce a pair of tomographic images. Consequently, between successive tomographic images, the Si camera has to wait during 2.5 s. As said before, accumulating a greater number of images would increase the time acquisition without significant improvements in detection sensitivity, due to mechanical drift in the setup.
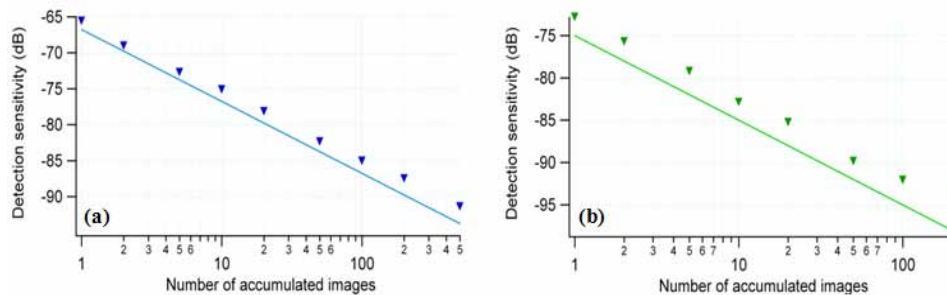
Fig. 3. Experimental detection sensitivity as a function of image accumulation for the Si (a) and the InGaAs (b) systems. The theoretical shot-noise limit is represented by the straight lines.

### 3.2 Axial resolution

Interference occurs only when the optical path length difference between the two interferometer arms is inferior to the coherence length of the illumination source. The axial resolution, which is generally defined as the full-width-at-half-maximum (FWHM) $\Delta z$ of the interferogram, is determined by the coherence length of the illumination source, inversely

proportional to the spectral bandwidth. Assuming the spectrum to be Gaussian-shaped and in the absence of dispersion and absorption, the axial resolution is given by

$$\Delta z = \frac{2\ln 2}{n\pi}\left(\frac{\lambda^2}{\Delta\lambda}\right),\tag{6}$$

where $n$ is the refractive index of the medium, $\lambda$ the center wavelength and $\Delta\lambda$ the effective optical spectrum width (FWHM), which is given by the product of the halogen lamp spectrum, the spectral transmission of the system optical components and the spectral response of the camera. With the assumption of no absorption, the effective optical spectrum width is essentially imposed by the spectral response of the cameras.

According to Eq. (6), the axial resolution decreases when the wavelength increases. To keep axial resolution constant, the spectral response width of detectors should increase like the square of wavelength. However, most long-wavelength detectors do not compensate the increase in wavelength by a sufficient spectral response broadening. The theoretical axial resolutions in water of both systems are listed in Table 1, calculated from Eq. (6) using the spectral characteristics of the cameras. The refractive index of water at both wavelengths was calculated using the Sellmeier formula [24]. As expected, the axial resolution with the Si CCD is better than with the InGaAs camera.

Table 1. Theoretical axial resolutions of the both optical systems in water calculated from Eq. (6).

|                             | Si camera | InGaAs camera |
| --------------------------- | --------- | ------------- |
| Center wavelength (nm)      | 820       | 1300          |
| Spectrum width (nm)         | 300       | 600           |
| **Axial resolution in water (µm)** | **0.75**  | **1.0**       |

When using water-immersion microscope objectives for biological sample imaging, the absorption by water cannot be neglected anymore. To study its effects on axial resolution, we have simulated the absorption by 6 mm of water (twice the working distance of our objectives), using the spectral response of both cameras and considering the optical transmission of water in these wavelength regions [23]. For the Si camera (see Fig. 4(a)), the spectrum shape is nearly unchanged by water absorption. Thus, the theoretical axial resolution in water can be calculated with Eq. (6), equal to 0.75 µm. In contrast, for the InGaAs camera (see Fig. 4(b)), water absorption limits the effective spectral range above 1400 nm (although the spectral response of the InGaAs camera extends to 1700 nm). As a consequence, the axial resolution is degraded. Simulations taking into account the effect of water absorption give an axial resolution of 1.4 µm instead of 1.0 µm calculated from Eq. (6). However, even if the absorption by water degrades the axial resolution, a configuration with water-immersion objectives is necessary to reduce dispersion mismatch and make dynamic focusing adjustments unnecessary. Indeed, with dry microscope objectives, as the object is translated in the axial direction to probe at different depths, the optical path in air is progressively replaced by an optical path in the biological sample. Thus, translation introduces dispersion between both arms of the interferometer, which degrades the axial resolution. Moreover, the image contrast is also degraded because the coherence plane moves away from the focal plane [9]. With water-immersion objectives, because the refractive index in most biological samples is close to that of water, these two phenomena are negligible.
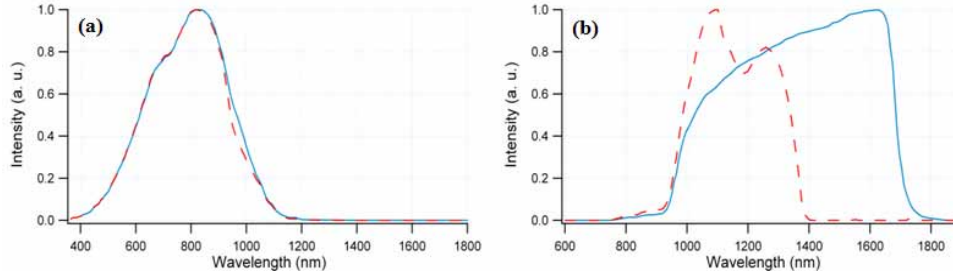
Fig. 4. Modelization of the absorption by water on Si (a) and InGaAs (b) responsivity. The blue straight curves correspond to responsivity without absorption and the red dotted curves to spectra after absorption by water.

We have measured the interferogram response of the system in water using a silver mirror in the object arm (see Fig. 5). The effective spectra are deduced from Fourier transform of the interferogram using a Hamming window for apodization. These spectra are in good agreement with the previous simulations (see Fig. 4). The wings in the InGaAs interferogram are due to the dips in the effective spectrum due to water absorption. The FWHM of the fringe envelope was found to be 0.8 µm for the Si setup and 1.5 µm for the InGaAs setup.
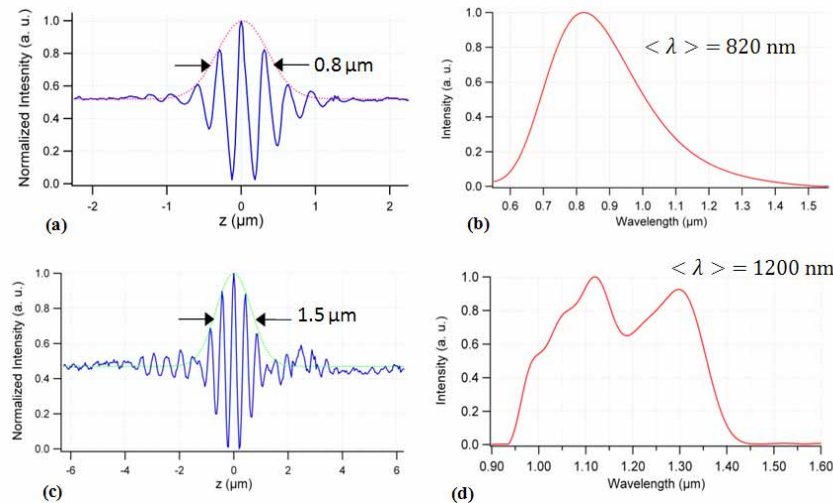


Fig. 5. Experimental measurements of the interferogram in water at 0.8 µm (a) and 1.2 µm (b). The effective spectrum of the system at 0.8 µm (c) and 1.2 µm (d) is calculated by Fourier transform.

### 3.3 Transverse resolution

The transverse resolution of an imaging system is commonly defined as the FWHM of the transverse point-spread function (PSF). Assuming the optical system to be diffraction-limited, the PSF is the well-known Airy function $h(u)$. The transverse resolution $\Delta r$ is then determined by the numerical aperture (*NA*) of the microscope objectives and the optical wavelength:

$$h(u) = \left| \frac{2J_1(u)}{u} \right|^2 \text{ where } u = \frac{2\pi}{\lambda} r NA \qquad (7)$$

$$\Delta r = \frac{\lambda}{2NA} \qquad (8)$$

Experimentally, we have measured the transverse resolution by recording an intensity profile across a cleaved mirror. Theoretically, the response is the convolution of a perfect edge and the PSF and a rectangular function (which simulates the image sampling by the camera pixels). The experimental 20 - 80 % width of this response (criteria which gives transverse resolution closed to expression (8) calculated with the center wavelength of the effective spectra) gives a theoretical transverse resolution of 1.7 µm and 2.0 µm for the Si and InGaAs setups respectively. Experimental results and theoretical calculations in water are presented in Fig 6. The experimental transverse resolutions are 1.8 and 2.5 µm for the Si and InGaAs setups respectively. The degradation between experimental and theoretical transverse resolution for the InGaAs setup is attributed to optical aberrations of the microscope objectives, which are not optimized in the 1200 nm wavelength region.
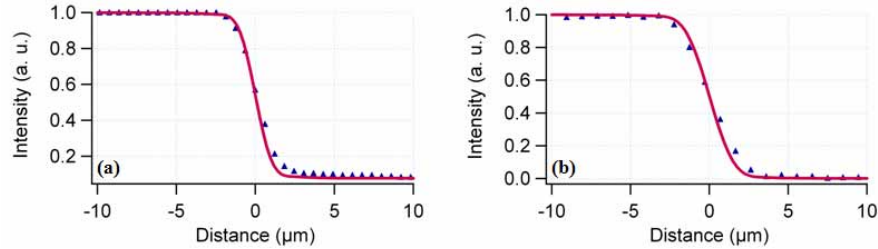


Fig. 6. Experimental measurements of the transverse resolution in water at 0.8 µm (a) and 1.2 µm (b). The blue markers correspond to measurements and the red line corresponds to the theoretical calculations (convolution of a perfect step and the PSF and a rectangular function).

## 4. Simultaneous dual-band FF-OCT imaging

### 4.1 Imaging penetration depth

In most biological tissues, scattering and absorption of light are the dominant factors that limit the imaging penetration depth.

Scattering is due to particles contained in the biological media. The intensity of light scattered by these particles depends strongly on their size and nature. Generally, this intensity varies with the optical wavelength $\lambda$ as $1/\lambda^k$ where $k$ is a parameter which depends on the size, geometry and refractive index of the scattering particles ($k > 1$). Thus the intensity of light scattered by biological samples decreases when wavelength increases [25-26].

Because water is the main constituent of biological media, absorption of light in these samples is dominated by water absorption. This absorption is minimal at the wavelength of 500 nm and globally increases with increasing wavelengths [23].

The optimal wavelength to maximize the OCT imaging penetration results from the best trade-off between absorption and scattering. Previous works have shown better penetration depth in highly scattering tissues for OCT operating in the 1200 nm wavelength region compared to 800 nm [26].

The effect of scattering on penetration depths was studied by imaging a mask for photolithography through 3 mm of 4% Intralipid solution commonly used to simulate scattering by biological tissues [27-28]. The reflection coefficient of the mask is almost independent of wavelength in the infrared region. Without Intralipid solution, images at both wavelengths have similar contrasts. When the sample is embedded in the Intralipid solution, the image constrast is considerably degraded at 800 nm whereas it is almost unaltered at 1200 nm due to the wavelength dependence of light scattering (see Fig. 7). In biological media, the situation is quite different because the intensity of light backscattered by the structures inside the imaged sample is also wavelength dependent.
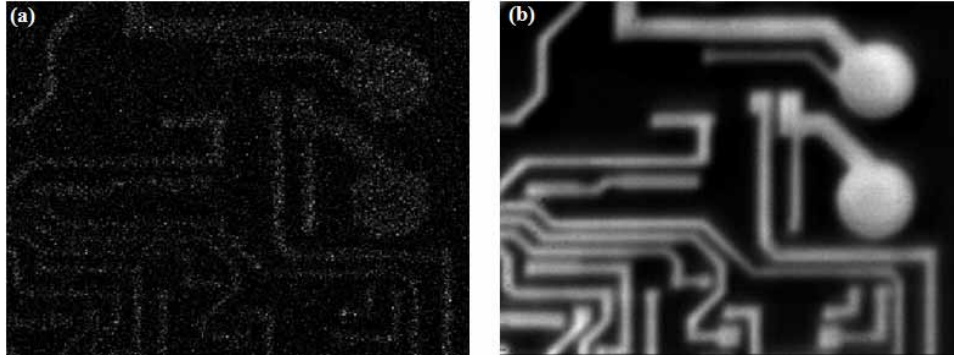
Fig. 7. FF-OCT images of a mask for photolithography acquired simultaneously in the 0.8 µm wavelength region with the Si camera (a) and in the 1.2 µm wavelength region with the InGaAs camera (b) through 3.1 mm thick Intralipid solution.

### 4.2 Images of biological samples

A large variety of *ex-vivo* animal tissues was imaged with our dual-band ultrahigh-resolution FF-OCT setup, with a drop of physiological serum inserted between the microscope objective and the samples. The experimental procedure consists of acquiring a stack of tomographic images at successive depths by moving the sample using a motorized translation stage with 1 µm steps. All the images presented here are in logarithmic scale. The black corresponds to the lowest signal and white to the highest.

Simultaneous dual-band FF-OCT imaging of the African frog tadpole *Xenopus laevis* was performed. A 250 µm × 1200 µm cross-sectional (XZ) image was extracted from a three-dimensional (3D) data-set acquired in the tadpole head. Images obtained at 800 and 1200 nm are displayed in Fig. 8(a) and 8(b) respectively. Epidermis, different stages of mesenchymal cells and stomach structures are revealed. As expected, the axial and transverse resolutions are better with the Si camera, for which the membrane and nucleus morphology of cells clearly appears. As seen before, the degradation of the axial and transverse resolutions at 1200 nm is due to respectively wings in the interferogram response, whose contribution is enhanced by the logarithmic scale, and optical aberrations of the microscope objectives. This degradation yields to blurred images with the InGaAs camera compared to the Si camera, which explains the slightly apparent difference between both images. On the other hand, a higher penetration depth is achieved with the InGaAs camera, for which the scattered structures of stomach (above 800 µm of penetration depth) are revealed.
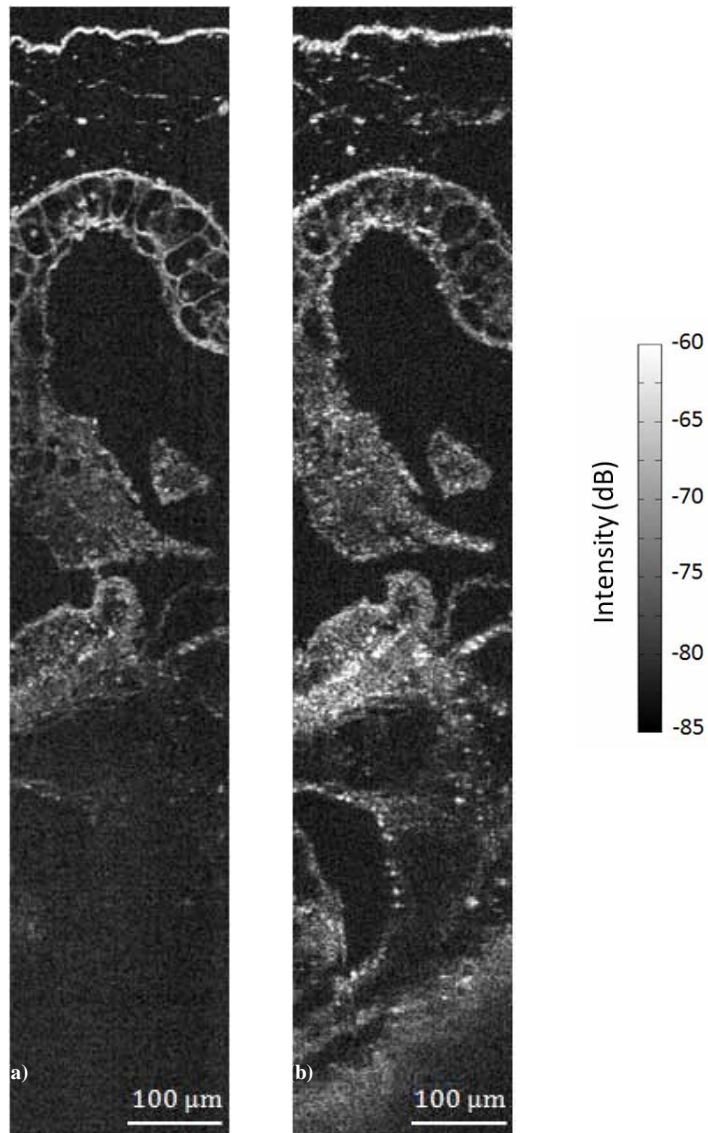
Si (0.8 µm)          InGaAs (1.2 µm)

Fig. 8. Dual band FF-OCT cross sectional images of the African tadpole *Xenopus laevis*, *ex vivo*, representing a volume of 250 µm × 250µm × 1200 µm at 800 nm (a) and 1200 nm (b).

As a second example, simultaneous dual-band FF-OCT of the rabbit trachea *ex vivo* is presented in Fig. 9, which shows a 250 µm × 400 µm cross-sectional (XZ) image. When comparing the fine structures in the single band images, like the cartilaginous ring above the epithelium, it is evident that the spatial resolution achieved at 800 nm is higher than at 1200 nm, as expected. In the other hand, there is an evident benefit in penetration depth at 1200 nm. For better visualization of the differences between both single band images, a color image representation was applied similar to the one presented in [16, 19]. We used a hue-saturation-luminance value mapping to represent the intensity and enhance the spectroscopic information content of the dual-band OCT images. To obtain this color image, both OCT images were normalized and hue-attribute was fixed (in green and red hues respectively for the 800 nm and the 1200 nm images). Then, the saturation and luminance attributes of the differential color map were set as the average OCT signal amplitude of both images. Thus, the

structures with higher intensity at 1200 nm image appear red in the color image, while structures which are dominant at 800 nm image are colored in green. Due to the degradation of the axial and transverse resolutions at 1200 nm, great care was taken for perfect image superposition. The color image is presented in Fig. 9(c). In the superficial layer, corresponding to the trachea epithelium, the backscattered light intensity is similar for both wavelength bands. In contrast, in the medium layer, the fibrous membrane structures have various wavelength dependant properties. At deeper depth, the image color turns to red, due to a better penetration depth at 1200 nm compared to 800 nm.
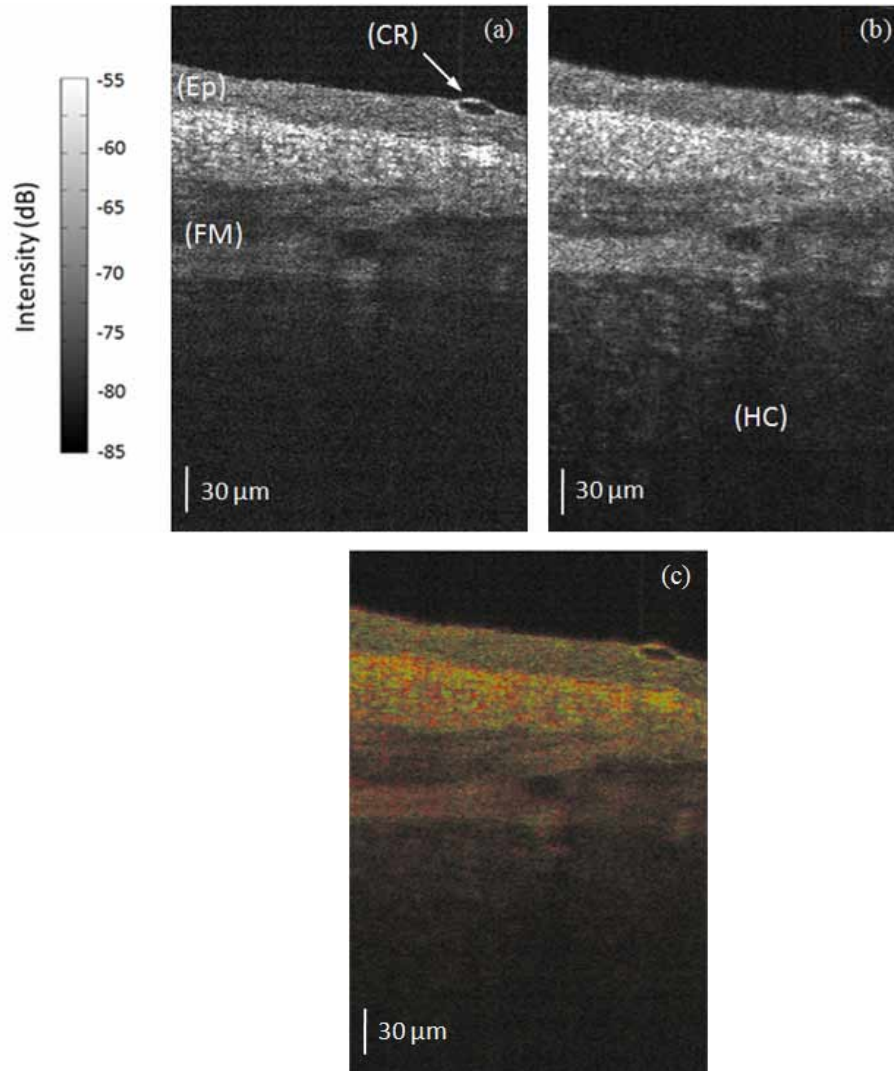


Fig. 9. Dual band FF-OCT cross sectional images of the rabbit trachea, *ex vivo*, representing a volume of 250 µm ×250 µm ×400 µm, at 800 nm (a) and 1200 nm (b). (c) represents the differential color image. Ep epithelium; CR cartilaginous ring; FM fibrous membrane and HC hyaline cartilage.

## 5. Conclusion

This paper presents dual-band ultrahigh-resolution FF-OCT based on a setup optimized to support two broad wavelength regions in parallel. Two *en-face* oriented tomographic images

can be recorded simultaneously in the wavelength regions centered at 800 nm and 1200 nm, with a detection sensitivity of ~ 90 dB. A spatial resolution within tissues of 0.8 µm × 1.8 µm and 1.5 µm × 2.5 µm (axial × transverse) are achieved at 800 nm and 1200 nm respectively. Significant improvement in imaging penetration depth was demonstrated at 1200 nm compared to 800 nm. A color image representation was applied to fuse both images in one single for better comparison of wavelength effects. This technique would allow a spectroscopic study of the wavelength dependence of the imaged sample. Compared to spectroscopic FF-OCT [16], dual-band FF-OCT provides spectroscopic measurements at only two wavelengths. On the other hand, spectroscopic FF-OCT requires the acquisition and processing of the entire interferometric signal by each CCD pixel. Consequently, dual-band FF-OCT offers a dramatic reduction of time acquisition and data processing, which would make possible FF-OCT with access to spectroscopic properties of the imaged tissues *in vivo*.

## Acknowledgment